PAPER

Lithium-metal all-solid-state batteries enabled by polymer-coated halide solid electrolytes

Pravin N. Didwal [ID] and Guoying Chen [ID] *

Halide solid electrolytes (HSEs) hold great promise for next-generation all-solid-state batteries (ASSBs); however, their application in practical devices is significantly hindered by their poor air and chemical stabilities and reactivities at the lithium–metal anode interface. In this study, we present a methodology involving the modification of HSEs with an ionically conductive and electronically insulating polymer composite, leading to enhanced stability against lithium metal and stable cycling of ASSB cells. The concept is exemplified through the fabrication of a poly(methyl methacrylate) (PMMA) modified Li_3YCl_6 (LYC) solid electrolyte (LYC_PMMA). Li symmetric cells employing LYC_PMMA exhibited stable lithium plating/stripping performance for well over 1400 cycles. In ASSB cells comprising an uncoated $LiNi_{0.8}Co_{0.1}Mn_{0.1}O_2$ (NMC811) cathode and a lithium metal anode, a discharge capacity of approximately 125 mAh g^{-1} was achieved at 1C cycling, with a coulombic efficiency of over 99.5% and a capacity retention of 99% over 100 cycles at RT. The polymer coating not only mitigates degradation reactions at the lithium metal anode interface but also enables cell cycling under a reduced external pressure and imparts air stability, thereby enhancing processability and manufacturability. This investigation introduces a facile and scalable approach for stabilizing halide electrolytes against lithium metal, offering a viable route to high-energy and cost-effective ASSB technologies.

Broader context

The global transition to sustainable energy demands advanced energy storage technologies that combine high energy density, safety, and scalability. Solid-state batteries have emerged as a leading contender for replacing conventional lithium-ion batteries, offering enhanced energy density and intrinsic safety benefits. Among solid electrolytes, halide-based materials show exceptional promise but are hindered by instability at the lithium metal interface and vulnerability to moisture in air, limiting their practical application. Addressing these challenges, we present a facile polymer coating strategy using poly(methyl methacrylate) to stabilize halide electrolytes, enabling long-term, reliable battery performance under low external pressures. This approach supports air-compatible processing, substantially reducing manufacturing complexity and cost and enhancing scalability. Moreover, the coating method is adaptable to diverse polymer systems, providing a versatile platform for broader battery material protection. By overcoming key barriers to solid-state battery commercialization, this work advances energy storage technologies critical for electric transportation and grid resilience, ultimately achieving energy independence.

1. Introduction

All-solid-state batteries (ASSBs) combining a 4 V-class cathode, a solid electrolyte (SE), and a Li metal anode are considered the future of energy storage technologies.[1,2] Unlike traditional Li-ion batteries (LIBs), ASSBs address the safety concerns by eliminating the use of flammable liquid electrolytes.[3,4] Additionally, ASSBs can achieve higher energy density due to improved cell unit stacking and the utilization of a Li metal anode.[5,6] Among various Li-ion conducting materials, sulfides and oxides are the most extensively studied SE candidates.

Sulfides exhibit high ionic conductivity and superior mechanical properties, but their drawbacks include poor chemical stability in humid air and incompatibility with conventional 4 V-class cathodes.[7–9] Oxides, on the other hand, offer a broader electrochemical stability window and better chemical stability; however, they are difficult to process and prone to brittleness and mechanical damage at the interfaces.[2,10,11]

Recently, halide solid electrolytes (HSEs) with the general formula Li_3MX_6 (M = In, Sc, Y, Er, etc.; X = Br, Cl, etc.) have garnered significant interest as a potential game changer for ASSBs.[12–14] Halides combine the advantages of sulfides and oxides in terms of processability and electrochemical stability at high voltages; however, they face significant challenges at the anode interface where severe degradation reactions occur.[13,15] The commonly present high-valence metal cations in

Energy Storage and Distributed Resources Division, Lawrence Berkeley National Laboratory, Berkeley, CA 94720, USA. E-mail: gchen@lbl.gov

HSEs are readily reduced to metallic M^0 upon contact with Li metal, leading to an electrically conductive interface layer that grows uncontrollably. The process consumes both the HSE and Li metal, causing eventual material depletion and short circuits in ASSBs.[15–17] Currently, strategies to address these issues are limited and they often involve the use of Li–M alloys (M = In, Sn, Ga *etc.*) to increase the anode operating voltage, resulting in a reduction in the overall ASSB energy density. A well-known example is the Li–In alloy anodes that operate at 0.62 V *vs.* Li. Another approach introduces a sulfide-based SE interlayer between the HSE and anode, such as lithium phosphorus sulfide (LPS) and lithium phosphorus sulfur chloride (LPSC) argyrodite.[18,19] However, the sulfide-based SEs are often chemically and electrochemically incompatible with HSEs, leading to surface degradation and increased interfacial resistance, which adversely affect long-term cycling performance.[20,21] In addition, the process of adding a sulfide-based SE increases the cost due to complexity in the processing and handling. Overall, the strategies developed so far all have met with limited success, with anode instability persisting as a major roadblock.

Solid polymer electrolytes (SPEs) have shown promise in ASSBs, offering enhanced safety, flexibility, and interfacial contact compared to inorganic SEs. Historically, SPEs suffer from low room-temperature (RT) ionic conductivities (typically $\sim 10^{-7}$–10^{-5} S cm^{-1}) and narrow electrochemical stability windows (<4 V), which hinder their application in high energy density ASSBs.[22] Recent efforts have focused on improving Li$^+$ transport through mechanisms such as decoupled ion transport, where Li-ion mobility is less dependent on polymer segmental motion, and on tailoring salt–host interactions. These advances, along with innovations in the polymer structure (*e.g.*, block copolymers, single-ion conductors) and formulation (*e.g.*, plasticizers, ionic liquids), have enabled SPEs to achieve RT ionic conductivities exceeding 10^{-4} S cm^{-1}, high Li-ion transference numbers ($t_{Li^+} \sim 0.8$), and oxidative stability up to 4.8–5.0 V, suitable for pairing with 4 V class cathodes like LiNi$_{0.8}$Co$_{0.1}$Mn$_{0.1}$O$_2$ (NMC811).[23–25] In addition, *in situ* polymerization and interfacial engineering strategies have been developed to produce thin, conformal, low-impedance interfaces with both Li metal and high voltage cathodes.[22] Several recent full-cell studies have demonstrated the effectiveness of such strategies. Li *et al.* reported a composite polymer electrolyte enabling 151 mAh g^{-1} at −20 °C in a Li/NCM811 pouch cell.[26] Zhang *et al.* employed a cellulose-supported SPE in a LiFe$_{0.2}$Mn$_{0.8}$PO$_4$/Li cell, achieving 96% capacity retention over 100 cycles at 20 °C.[27] Pazhaniswamy *et al.* fabricated a PVDF/Al-LLZO hybrid SPE that enabled an LFP/Li cell to deliver 159 mAh g^{-1} at 0.5 C for 120 cycles at 25 °C.[24] Despite these advances, SPEs still face challenges such as sustaining high RT conductivity without compromising mechanical strength, maintaining stable operation at elevated current densities, and achieving scalable, defect-free processing for commercial cell formats.

Here we developed an approach that utilizes an SPE as a protective coating layer to mitigate the detrimental interactions between the HSE and the Li metal anode, enabling chemically- and electrochemically-stable interfaces. While similar approaches have been demonstrated in ASSBs with other SEs such as argyrodites, hydrides, and oxides, most studies focused on the polymer interfaces between the SE and a Li-alloy-based anode, with only a few examples exploring their compatibility with a Li-metal anode (Table S1). As far as we know, the application of polymers as a direct coating on HSE particles has not yet been reported, especially in conjunction with a Li metal anode. In the current approach, the desirable polymers are those with low electronic conductivities, excellent room temperature (RT) ionic conductivities, good electrochemical stability at the low potential of Li metal, and robust mechanical strength.[28–32] One such example is poly (methyl methacrylate) (PMMA), which is widely available and has been extensively studied in LIBs. Here PMMA–LiTFSI was chosen as an interfacial coating driven by a strategic combination of its chemical, electrochemical, and mechanical properties. Although pristine PMMA has a relatively low Li-ion conductivity, incorporating a small amount of LiTFSI (15 wt%) provides a significant boost for Li$^+$ transport across the thin layer. A key advantage is the material's electronic insulation, which suppresses the reduction of Y^{3+} and the formation of conductive interphases (*e.g.*, metallic Y, LiCl) – primary failure mechanisms at the Li|LYC interface. Furthermore, PMMA offers high electrochemical stability at low potentials, hydrophobicity for moisture resistance during processing, and mechanical softness to improve Li wetting and homogenize stack pressure. Together, these attributes make PMMA–LiTFSI an effective, multifunctional barrier. We show that by coating Li$_3$YCl$_6$ (LYC) SE particles with a thin layer of PMMA–LiTFSI using a mechanochemical method, the resulting composite (referred to as LYC_PMMA) significantly reduces the interfacial resistance and enables long-term lithium plating/stripping for over 1400 cycles under a low stack pressure of ∼5 MPa. Excellent performance was achieved on ASSB cells equipped with an uncoated LiNi$_{0.8}$Co$_{0.1}$Mn$_{0.1}$O$_2$ (NMC811) cathode and a Li metal anode. For the first time we demonstrate the use of a PMMA interfacial coating on HSE particles to achieve: (1) enhanced Li-metal compatibility by suppressing interfacial decomposition reactions that lead to LiCl formation and Y^{3+} reduction, (2) improved moisture resistance due to the hydrophobic nature of PMMA, enabling better handling and processability under ambient conditions, and (3) higher energy density enabled by the combination of a Li metal anode and a high voltage cathode. We further obtained a mechanistic understanding using synchrotron-based micro X-ray fluorescence (µXRF) mapping, hard X-ray absorption (hXAS) analysis, *in situ* grazing incidence X-ray diffraction (GIXRD), and X-ray photoelectron spectroscopy (XPS) analysis.

2. Results and discussion

2.1. Synthesis and properties

The PMMA-modified HSE was synthesized *via* a mechanochemical method at room temperature under an Ar atmo-

sphere. To enhance Li-ion conductivity, lithium bis(trifluoro-methanesulfonyl)imide (LiTFSI) was incorporated into PMMA (PMMA : LiTFSI = 85 : 15 wt%) prior to the coating process. Fig. 1a shows the X-ray diffraction (XRD) patterns of PMMA, LYC, and LYC_PMMA, obtained using synchrotron XRD in the transmission mode (wavelength converted to Cu Kα, 1.54 Å in Fig. 1a). The XRD pattern of PMMA displays a single broad peak, typical of its amorphous nature.[33] The pristine LYC exhibits a trigonal structure with well-defined XRD peaks, consistent with the results previously reported.[13] The XRD pattern of LYC_PMMA shows that the trigonal structure of LYC remains intact after the coating process, although the intensity of the diffraction peaks somewhat decreases. The reduction is consistent with the presence of the amorphous PMMA coating on the LYC surface, which dampens the XRD signals. In addition, the high-energy milling process may reduce the crystallite size and induce micro-strain and minor structural disorder at the particle surfaces, all of which can contribute to the reduction in peak intensity. Fig. 1b and c compare the scanning electron microscopy (SEM) images of the LYC and LYC_PMMA particles. The pristine LYC particles (Fig. 1b) are fairly non-uniform in size and shape, characteristic of samples prepared using the high-energy ball milling method. Surface roughing and wrinkle-like features are clearly shown on LYC_PMMA particles (Fig. 1c), indicating the presence of the PMMA polymer coating. Furthermore, energy-dispersive X-ray spectroscopy (EDS) line mapping reveals small amounts of carbon (C) and oxygen (O) evenly distributed across the particles (Fig. S1a and b), which can be attributed to the presence of the polymer.

The low levels of C and O detected are consistent with a thin polymer coating layer on the surface of LYC particles (Fig. S1c).

Fig. 1d compares the Fourier-transform infrared (FTIR) spectra of LYC, PMMA, and LYC_PMMA. The spectrum of pure PMMA displays characteristic absorption bands at ~1730 cm^{-1} and 1145 cm^{-1}, corresponding to the C=O stretching vibration of ester groups and C–O–C stretching, respectively. In contrast, the spectrum of pure LYC shows no significant peaks in these regions, as expected for the inorganic halide material lacking organic functional groups. In the LYC_PMMA spectrum, the absorption bands corresponding to PMMA are clearly visible, albeit with reduced intensity, confirming the successful incorporation of PMMA onto the LYC particles. The shift of the C=O bands towards lower wavenumber is likely a result of chemical interactions between LYC and the PMMA, suggesting the nature of an intermediate coating layer on the surface. On the thermogravimetric analysis (TGA) profiles (Fig. S1d), LYC_PMMA shows a minor initial weight loss above 100 °C, which can be attributed to the loss of surface moisture. A subsequent gradual weight loss of ~5.37% corresponds to the thermal decomposition of the PMMA component, indicating that the composite contains approximately 5.37 wt% PMMA, closely matching the targeted composition during synthesis. Compared to pure PMMA, the delayed onset and broader decomposition profile in the composite suggest enhanced thermal stability, likely due to interfacial interactions between PMMA and LYC. Based on the average particle size, densities, and weight ratios of LYC and PMMA, the estimated PMMA coating thickness was calculated to be approximately 4.3 nm
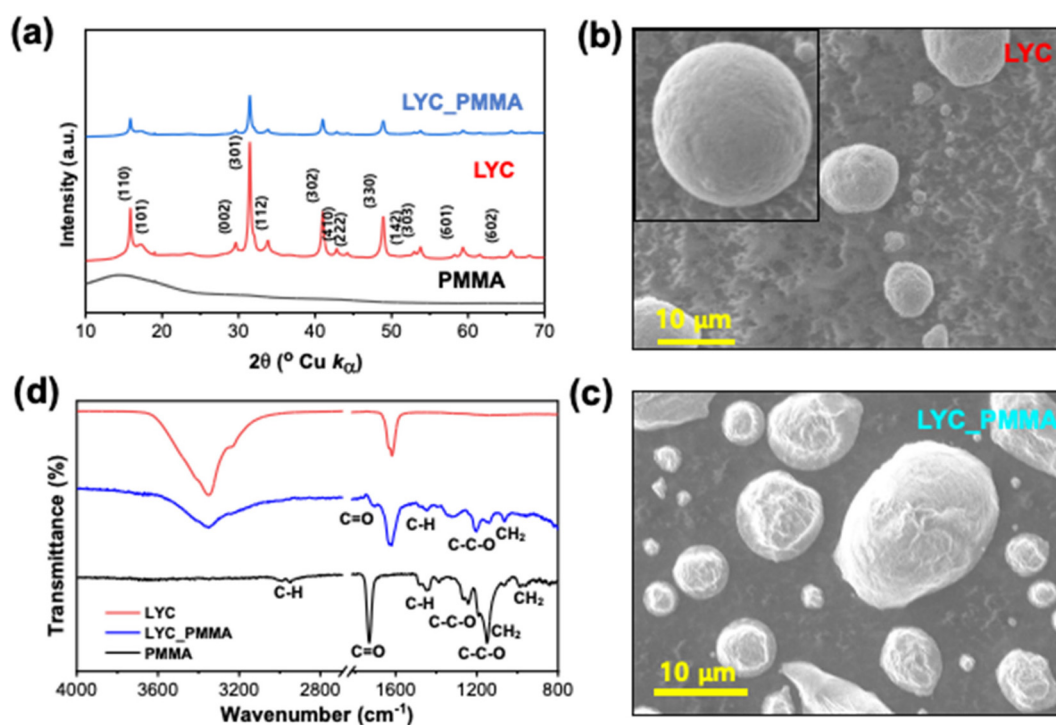

Fig. 1 (a) XRD patterns of PMMA, LYC and LYC_PMMA. SEM images of LYC (b) and LYC_PMMA (c). (d) FTIR spectra of PMMA, LYC and LYC_PMMA. The intensity of the LYC spectrum was reduced by 10 times for better comparison.

(SI Note 1). This value is further supported by XPS analysis presented in the following section.

The surface chemical state of the sample was further evaluated using XPS analysis. Fig. S2 compares the Y 3d, Cl 2p, and Li 1s spectra collected on the pristine and PMMA-coated LYC, respectively. The Y 3d spectra for the pristine (Fig. S2a) show two peaks corresponding to Y $3d_{5/2}$ and Y $3d_{3/2}$, characteristic of the Y^{3+} oxidation state in LYC. In LYC_PMMA (Fig. S2b), these peaks remain at similar binding energies but exhibit lower overall intensity, consistent with the damping effect of the polymer coating. Similarly, the Cl 2p spectra from LYC display two peaks associated with Cl $2p_{3/2}$ and Cl $2p_{1/2}$, corresponding to the Cl^- state (Fig. S2c). No additional Cl features were observed after coating, aside from a decrease in intensity (Fig. S2d). The Li 1s spectra also show a single peak for both LYC and LYC_P, again with reduced intensity but no shift in binding energy (Fig. S2e and f). The uniform reduction in peak intensity across all spectra for LYC_PMMA further confirms the presence of a thin PMMA coating on the LYC surface without altering its chemical composition.

Ionic conductivities (σ) of the samples were measured using the ambient temperature (AT) electrochemical impedance spectroscopy (EIS) of a stainless-steel (SS) split cell equipped with either an LYC pellet or an LYC_PMMA pellet (approximately 354 ± 1 μm in thickness, Fig. S3a). Fig. S3b shows the Nyquist plots of the SS|LYC|SS and SS|LYC_PMMA|SS cells, respectively. The σ value of the LYC_PMMA pellet was determined to be 0.16 mS cm^{-1}, which is slightly lower than that of uncoated LYC (0.35 mS cm^{-1}). This reduction in conductivity is expected as the PMMA coating has a lower AT ionic conductivity which leads to a decrease in the overall conductivity of LYC_PMMA. The fitted equivalent circuit reveals contributions from both bulk and grain boundary resistances. Notably, LYC and LYC_PMMA show similar bulk resistance ($R_b = 91.2$ Ω). However, LYC_PMMA exhibited a higher grain boundary resistance ($R_{gb} = 192.7$ Ω) compared to that of pristine LYC ($R_{gb} = 38.1$ Ω). The ionic conductivity as a function of temperature and the Arrhenius plots are further compared in Fig. S4. The linear behavior is characteristic of thermally activated ion transport. The activation energies were determined to be 0.394 eV for LYC and 0.452 eV for LYC_PMMA. The slightly higher activation energy in the latter suggests that the PMMA coating introduces an additional barrier in Li-ion migration, which is expected.

We further evaluated the effects of processing parameters on ionic conductivity. Fig. S5a compares the results obtained on LYC_PMMA samples prepared with 5 h, 10 h, and 20 h of ball milling, respectively, using the same speed of 300 rpm. The measured ionic conductivities are 0.12, 0.16, and 0.071 mS cm^{-1} for 5 h, 10 h, and 20 h, respectively. It is clear that 10 h of milling produces samples with the highest conductivity. We observed a change in color for the 20 h milled samples, suggesting degradation due to excessive milling. In addition, LYC with 10 wt% PMMA coating was also prepared and its conductivity was measured using EIS (Fig. S5b). The obtained value (0.08 mS cm^{-1}) was noticeably lower compared to that of 6 wt% PMMA coating (0.16 mS cm^{-1}).

2.2. Electrochemical performance

We first evaluated the role of applied stack pressure in the properties and performance using EIS measurements carried out under various stack pressures ranging from 2 to 22 MPa. The Nyquist plots and the relationships between the various resistance components and the stack pressure of the Li|LYC_PMMA|Li symmetric cell are shown in Fig. 2a and b, respectively. The bulk resistance of the SE (R_e) remains largely constant across the various stack pressures, consistent with the nature of the dense pellet. As expected, increasing the stack pressure significantly reduces the interfacial resistance (R_i), indicating improved contact between LYC_PMMA and Li metal. As a result, the total resistance (R_t) also decreases with an increase in stack pressure. Applying pressures above 22 MPa, however, caused the soft Li metal to creep, ultimately shorting the cell. The R_i and R_t values as a function of stack pressure are listed in Table S2.

The maximum extractable capacity under various stack pressures was evaluated using unidirectional Li stripping measurements. Fig. 2c displays the voltage profiles of the Li|LYC_PMMA|Li cell during continuous stripping under a current density of 1 mA cm^{-2} and a stack pressure from 2 to 22 MPa. Lowest capacities were obtained under either 2 or 22 MPa, whereas similar performances were obtained between these two values. Fig. 2d shows the areal capacity and polarization potential as functions of the stack pressure. The cells delivered areal capacities of 6.4, 13.6, 12.7, 12.4, and 7.4 mAh cm^{-2} at a stack pressure of 2, 5, 8, 14, and 22 MPa, respectively. The corresponding polarization potentials were 0.92, 0.44, 0.53, 0.63, and 0.76 V. The highest capacity and lowest polarization potential occurred at a stack pressure of 5 MPa, suggesting that this is near the optimal pressure for the interface with the lowest resistance between the Li metal and LYC_PMMA. We wish to point out that 5 MPa is a notably lower value compared to those reported in the literature.[34–36] Most halide-based SE cells operate with a stack pressure between 7 and 40 MPa in order to utilize the majority of cell capacity and achieve stable cycling.[37] We believe that the presence of the polymer interlayer provides a mechanically soft buffer layer that homogenizes the pressure across the interface between LYC and Li metal, hence lowering the overall stack pressure. Since the need for a high stack pressure is a significant concern for the integration of ASSBs into practical devices, the results highlight a significant advantage of our approach.

To understand the electrochemical stability of the LYC and LYC_PMMA in contact with Li metal, cyclic voltammetry (CV) was performed using Li|LYC|LYC-C and Li|LYC_PMMA|LYC_PMMA-C cells at a scan rate of 0.1 mV s^{-1}. For the LYC cell, a strong cathodic current initiated at ~1.8 V followed by a rapid increase at ~0.9 V vs. Li$^+$/Li (Fig. 3a), indicating the onset of electrolyte decomposition due to the reduction reactions (commonly attributed to the reduction of Y^{3+}) at the Li|LYC interface. In contrast, the LYC_PMMA cell exhibits a significantly reduced current response across the entire scanned
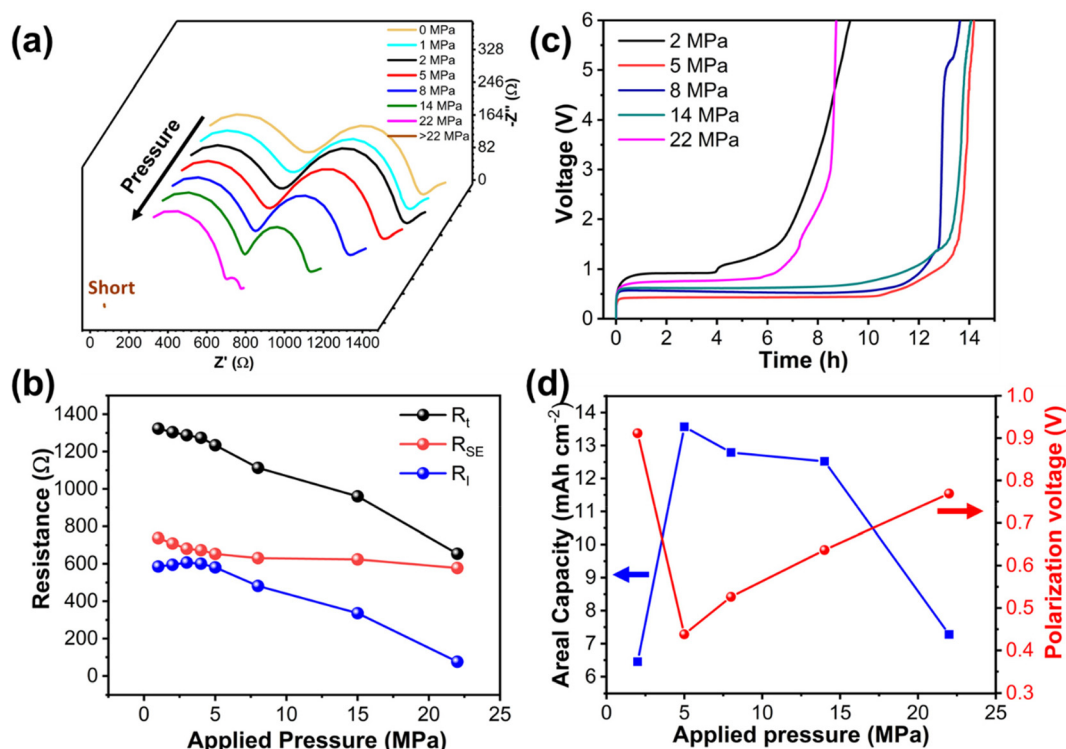
Fig. 2 (a) EIS profiles and (b) the relationships between various resistance components and the applied stack pressure of a Li|LYC_PMMA|Li cell, (c) voltage profiles during unidirectional stripping of Li|LYC_PMMA|Li cells under various stack pressures, and (d) areal capacity and polarization potential as a function of applied stack pressure.

voltage range of 0–2.5 V, with no observable large redox peaks. This behavior demonstrates enhanced electrochemical stability and passivation at the Li interface. The absence of decomposition features confirms the effectiveness of the PMMA coating in preventing the direct contact between Li metal and LYC, thereby mitigating interfacial degradation. These results provide strong evidence that surface modification with PMMA improves the electrochemical stability of LYC against Li metal, making LYC_PMMA a more reliable candidate for low voltage operation in ASSBs to increase overall energy density.

Establishing the critical current density (CCD) of the ASSB cell is essential for achieving stable cycling. To this end, we conducted continuous stripping/plating studies on Li|LYC|Li and Li|LYC_PMMA|Li symmetric cells with the current density ranging from 0.02 to 5 mA cm^{-2} (Fig. 3b). The Li|LYC|Li cell displays an unstable voltage profile beyond 0.5 mA cm^{-2}. In contrast, the Li|LYC_PMMA|Li cell exhibits lower polarization and better interface stability, even at a high current density of well over 1 mA cm^{-2}. We further assessed the long-term electrochemical stability of Li|LYC|Li and Li|LYC_PMMA|Li symmetric cells by performing repeated stripping/plating cycling at a current density of 0.5 mA cm^{-2} (Fig. 3c–e). The measurements were carried out under a stacking pressure of 5 MPa, with each cycle corresponding to 1 hour. Initially, the Li|LYC_PMMA|Li cell exhibited a slightly higher polarization compared to that in the Li|LYC|Li cell, likely due to the lower ionic conductivity of LYC_PMMA at ambient temperature.

However, the former cell demonstrated smooth and stable cycling for well over 1400 cycles, whereas the latter experienced a sharp increase in polarization after just 300 cycles (Fig. 3c). The voltage profiles also experienced gradual changes as opposed to the stable profiles maintained in the Li|LYC_PMMA|Li cell (Fig. 3d and e). The improved performance may be attributed to a synergistic effect of reduced interfacial resistance between LYC_PMMA and Li metal, along with enhanced stability at lower potentials compared to pristine LYC. While LYC undergoes degradation reactions at the low potential of Li metal, leading to increased polarization over time and ultimately resulting in short-circuiting, PMMA has better electrochemical stability against Li metal.[37,38] A detailed investigation of the underlying mechanism was carried out using *ex situ* XAS, μ-XRF, and XPS analyses, and the results are discussed in the following section.

In addition, the electrochemical behavior of Cu||Li half-cells assembled with two different electrolytes, LYC and LYC_PMMA, was evaluated under galvanostatic cycling (Fig. S6a and b). Both cells were cycled at a constant current density of 0.5 mA cm^{-2}, with Li plating set for 1 hour and stripping voltage limited to 1.0 V *vs.* Li/Li$^+$. During the first plating cycle, both electrolytes exhibited nearly identical voltage profiles. However, in the LYC cell, only 61% of the plated Li was reversibly stripped, indicating poor initial coulombic efficiency (ICE). Subsequent cycles showed a rapid increase in voltage polarization, with full capacity loss in just 4
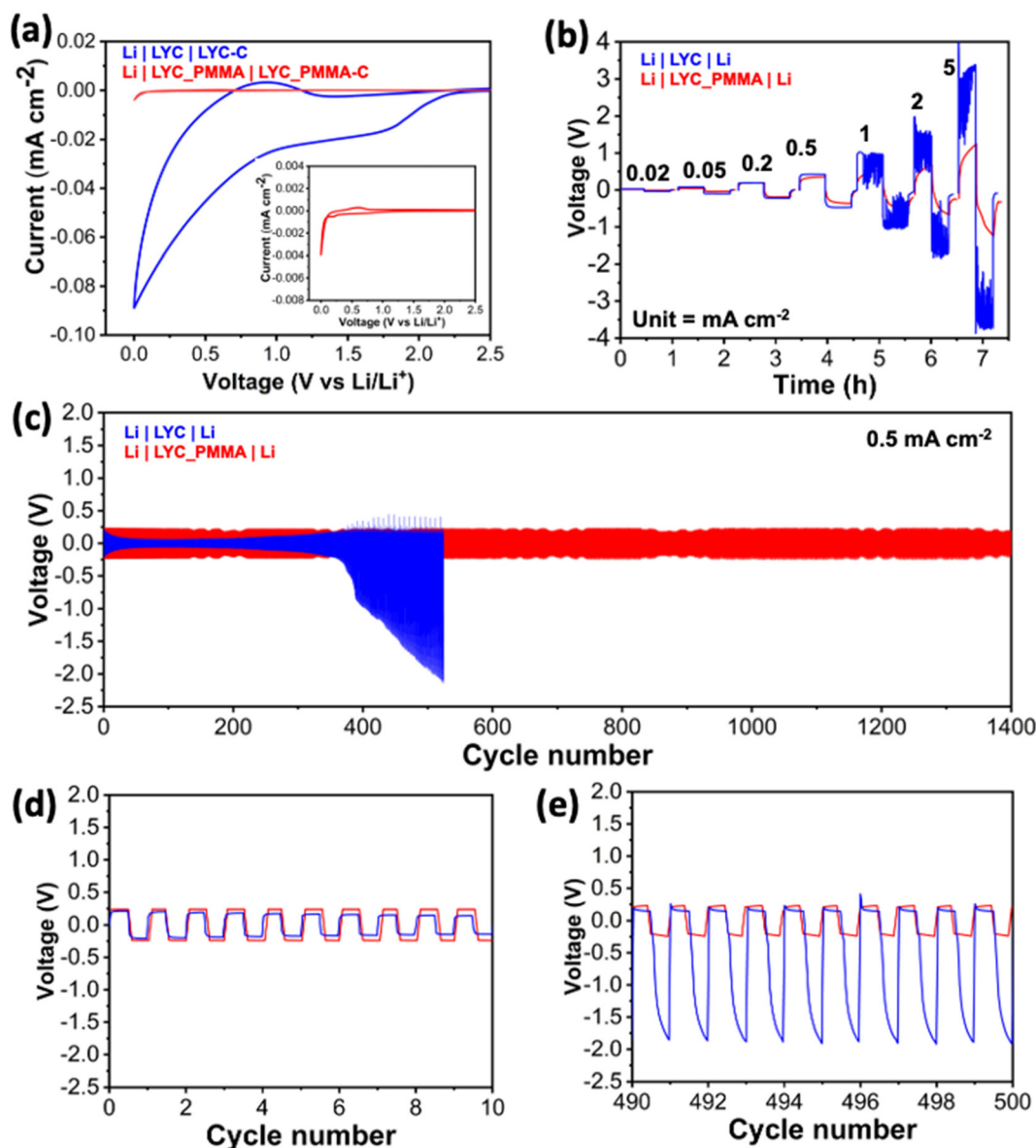
Fig. 3 (a) Cyclic voltammograms of Li|LYC|LYC-C and Li|LYC_PMMA|LYC_PMMA-C cells at a scan rate of 0.1 mV s^{-1}, (b) continuous stripping/plating of Li|LYC|Li and Li|LYC_PMMA|Li cells at various current densities ranging from 0.02 to 5 mA cm^{-2}, and (c−e) long-term stripping/platting performance of the Li|LYC|Li and Li|LYC_PMMA|Li cells at a current density of 0.5 mA cm^{-2} and a stacking pressure of 5 MPa. 1 full cycle is for 1 hour. (d and e) are the expanded views of the cycling profiles shown in Fig. (b). All measurements were carried out at room temperature.

cycles. The poor reversibility and sharp drop in CE are attributed to severe chemical and electrochemical instability between LYC and the Li metal surface. In contrast, the LYC_PMMA cell displayed significantly improved cycling performance (Fig. S6c). The corresponding Cu||Li half-cell maintained high CE and stable voltage profiles throughout extended cycling under identical conditions. The ICE of 91.7% further increased to 98.3% in the subsequent cycles. The excellent performance highlights the enhanced chemical stability and interfacial compatibility of the PMMA-coated LYC with Li metal, effectively mitigating parasitic reactions and suppressing polarization.

We further evaluated the performance of an ASSB full cell consisting of an uncoated NMC811 cathode active material (CAM), an LYC or LYC_PMMA SE, and a Li metal anode. The cathode composites were prepared by hand-grinding sc-NMC811 powder, LYC powder, and a conductive carbon additive in a weight ratio of 58 : 37 : 5. To take advantage of the HV stability of LYC and the low-voltage stability of LYC_PMMA against a Li metal anode, a bilayer cell configuration was used where the LYC layer (~300 μm) interfaced with the cathode and the LYC_PMMA layer (~100 μm) interfaced with the anode (Fig. S7a). To evaluate interfacial resistance, we first performed EIS measurements under various stacking pressures ranging

from 0 to 8 MPa. The cells exhibited a high interfacial resistance at 0, 1, and 2 MPa (Fig. S7b); however, the values were significantly reduced at 5 MPa, with well-defined semi-circle features observed at higher frequencies. On the other hand, the cell short-circuited at higher pressures, above 8 MPa. The ASSB full cell cycling study was then carried out at 5 MPa and ambient temperature (19 ± 6 °C), similar to the conditions used for the symmetric cell testing.

The rate capability of the LYC_PMMA cell was evaluated using constant current cycling with the rate ranging from 0.05C to 2C, followed by 0.1C cycling (1C = 200 mAh g^{-1}). As shown in Fig. 4a and b, the cell exhibited an increase in

capacity during the initial cycles at 0.05C, a result of the well-known "break-in" process in ASSBs, which was also observed in our previous studies.[12] The cell delivered a high discharge capacity of 172 mAh g^{-1} at 0.1C, suggesting excellent cathode utilization and good interfacial contact with Li metal. As the current density increased to 0.2C, 0.5C, 1C, and 2C, the cell delivered a discharge capacity of approximately 162, 148, 121, and 91 mAh g^{-1}, respectively. Although a gradual capacity decrease is typically observed for solid-state systems under higher currents, owing to limited Li$^+$ transport and increased interfacial resistance, the LYC_PMMA cell was able to maintain its capacity even at the 2C rate. These results highlight the ben-
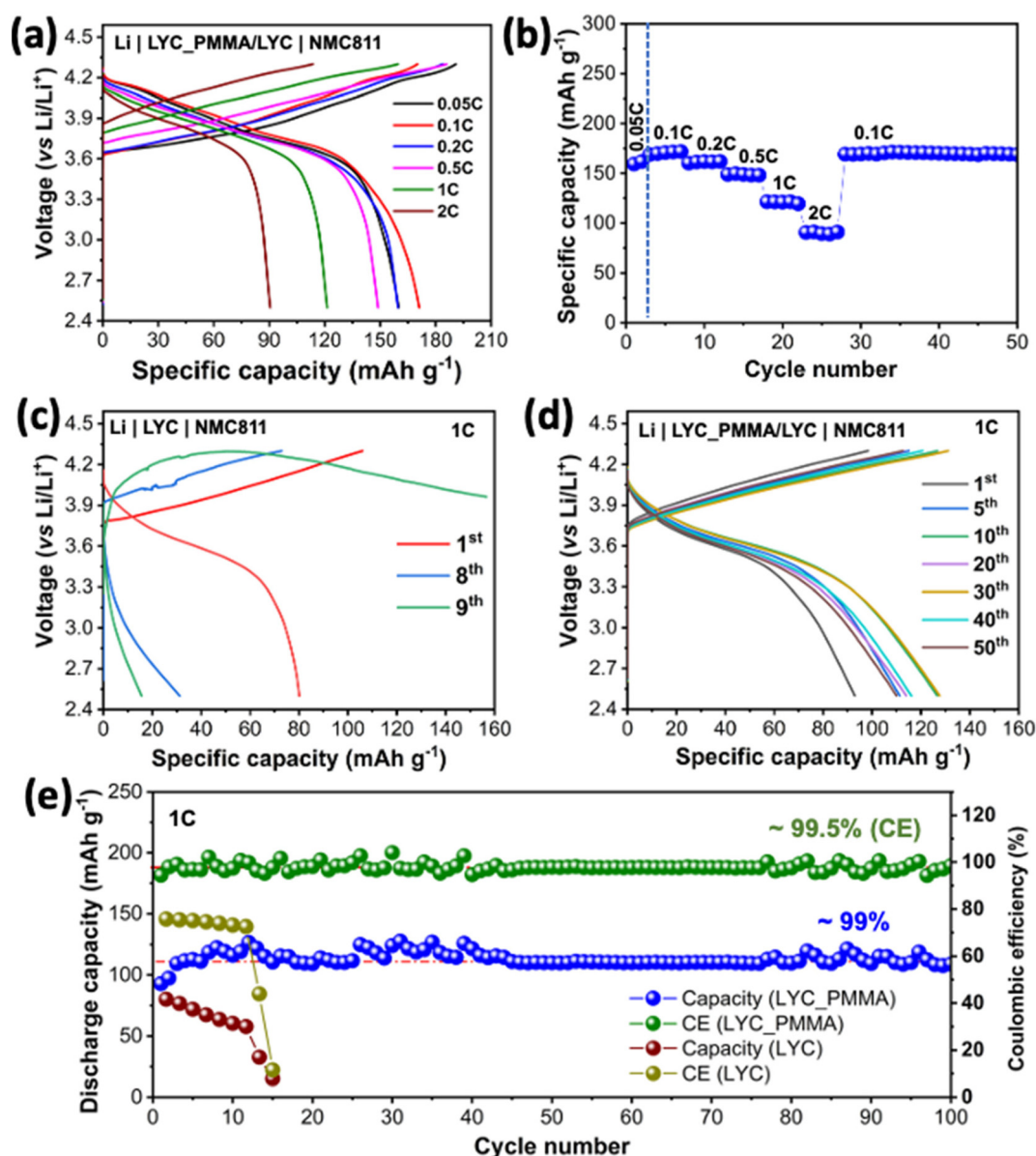

Fig. 4 (a) Galvanostatic charge–discharge profiles and (b) discharge capacity of Li|LYC_PMMA/LYC|NMC811 cells cycled at various rates as indicated (1C = 200 mAh g^{-1}). Galvanostatic charge–discharge profiles of (c) Li|LYC|NMC811 and (d) Li|LYC_PMMA/LYC|NMC811 cells cycled at the 1C rate, and (e) discharge capacity and coulombic efficiency as a function of cycle number for the Li|LYC|NMC811 and Li|LYC_PMMA/LYC|NMC811 cells cycled at 1C.

eficial role of the PMMA coating in promoting Li$^+$ transport and maintaining good electrode–electrolyte contact. Notably, the rate performance reported here surpasses the results reported in the literature (Table S1) as well as our previous reports using an LYC SE and a Li–In alloy anode.[13] Upon returning to 0.1C, the capacity nearly recovered to its initial value, suggesting that minimal degradation occurred during the high-rate cycling. The results further confirm that the reduced capacity observed at higher rates is predominantly due to kinetics instead of irreversible decomposition or interfacial instability.

Fig. 4c and d compare the galvanostatic charge/discharge voltage profiles of the Li|LYC|NMC811 and Li|LYC_PMMA/LYC|NMC811 full cells, respectively. The NMC811 active material mass loading was 5.38 mg cm^{-2}. At 1C rate, the LYC cell delivered first charge and discharge capacities of 106.6 and 80.1 mAh g^{-1}, respectively, corresponding to a coulombic efficiency (CE) of 75.7%. The subsequent cycles exhibited a continuous increase in electrochemical polarization, with the charging curve failing to reach the upper cutoff voltage of 4.3 V after 9 cycles. The behavior likely results from the decomposition of LYC due to the reactivity between the freshly deposited Li and LYC during the delithiation process. In contrast, the LYC_PMMA cell delivered first charge and discharge capacities of 98.6 and 93.1 mAh g^{-1}, respectively, a significant improvement in CE (94.4%). After the initial "break-in" process, the capacity increased to a maximum of nearly 130 mAh g^{-1} at the 8th cycle. Aside from the minor capacity fluctuations due to the variation in the AT, the cell demonstrated stable cycling with a capacity retention of nearly 99% and a CE of 99.4% after 100 cycles (in Fig. 4e, the red dotted line indicates the average capacity value obtained on the cells). To the best of our knowledge, these results represent one of the most stable cycling performances achieved by cells combining an HV-cathode such as NMC811, an HSE, and a Li metal anode (Table S1), highlighting the superior electrochemical stability of LYC_PMMA against Li metal anode and the efficacy of our approach in enabling Li-metal-based high-energy ASSBs.

Fig. S6c compares the EIS results of the LYC and LYC_PMMA ASSB cells before and after cycling. The measurements were taken after 9th and 100th cycles under the same conditions, respectively. The LYC cell exhibits a significantly larger semicircle before cycling, indicating high initial interfacial resistance due to poor contact between LYC and Li metal. After cycling, the total impedance further increases drastically, resulting from the interfacial reactions and the decomposition of the electrolyte. In contrast, the LYC_PMMA cell shows markedly lower interfacial resistance, both before and after cycling. There was no significant increase in the impedance, particularly after 100 cycles, which confirms that the PMMA layer facilitates improved Li-ion transport and maintains better interfacial contact during cycling by reducing the side reactions at the interface. These results clearly demonstrate the stabilizing effect of the PMMA coating on LYC, highlighting its role in mitigating interface degradation and enhancing electrochemical performance in ASSBs.

2.3. Mechanistic understanding

To understand the impact of the coating on LYC, we first evaluated elemental distribution using synchrotron micro μXRF mapping and chemical distribution using hXAS analysis at the Stanford Synchrotron Radiation Lightsource (SSRL). Fig. 5 compares the results collected on the cross-section of the SE pellets recovered from the Li|LYC|Li and Li|LYC_PMMA|Li symmetric cells after cycling at 0.5 mA cm^{-2}. Both LYC (Fig. 5a and b) and LYC_PMMA (Fig. 5c and d) showed uniform distribution of Y and Cl throughout the bulk of the pellets. While the LYC_PMMA pellet exhibited a clean and continued uniform distribution of Cl at the edge towards the Li electrode, an additional Cl-rich layer was observed at the interface between LYC and Li (marked by the dotted line in Fig. 5b). This is clearly shown by the color contrast in the composite μXRF maps of the Y K-edge and Cl K-edge (Fig. 5e), where the green color represents the layer with the Cl-rich nature. Based on our previous studies, the Cl-rich layer likely contains LiCl, the main product resulting from the decomposition reactions between LYC and Li metal during electrochemical cycling.[15,39] The same Cl-rich layer is notably absent in the recovered LYC_PMMA pellet (Fig. 5d–f), indicating that the PMMA coating effectively suppresses the decomposition reactions, enhancing the chemical and electrochemical stability of the SE against Li metal.

Fig. 5g and h compare the Y K-edge X-ray absorption near-edge structure (XANES) spectra collected at various positions across the cross-sections of the recovered LYC and LYC_PMMA samples, respectively. The measurements were performed at the selected points using a focused synchrotron X-ray beam with a spot size of 2 × 2 μm. The sample locations are denoted as L1 to L5 in the LYC pellet (Fig. 5e) and P1 to P5 in the LYC_PMMA pellet (Fig. 5f). Reference spectra for Y^0 and Y^{3+} were collected from Y foil and pristine LYC powder, respectively. In the LYC spectra, the Y K-edge profiles for L1 and L5 are well aligned with the Y^0 region (Y metal), while the spectra for L2, L3, and L4 are similar to that of Y metal and show an energy edge adjacent to that of Y^0. This indicates that cycling LYC with Li metal in the symmetrical cell led to the reduction of Y^{3+} to Y^0, forming a metallic Y phase that is present throughout most of the SE pellet. In contrast, in the cycled LYC_PMMA pellet, the Y K-edge spectra for P1 and P5 only slightly shifted towards lower energies. The spectra for P2, P3, and P4 remained entirely within the Y^{3+} region, confirming that the PMMA coating prevented the reduction of Y^{3+} to Y^0, with only a minor reduction occurring in the SE.

To further identify the nature of degradation products in both cells, surface-sensitive XPS measurements were also carried out. Fig. 5i and j compare the Cl 2p, Y 3d, and Li 1s spectra collected from the recovered LYC and LYC_PMMA pellets, respectively. The corresponding spectra collected on the pristine SE pellets are shown in Fig. S2a and b, respectively. In the Y 3d spectra, two primary peaks corresponding to Y^{3+} (3d$_{5/2}$ and 3d$_{3/2}$) are observed for both pristine LYC and LYC_PMMA. However, after cycling, LYC exhibits additional
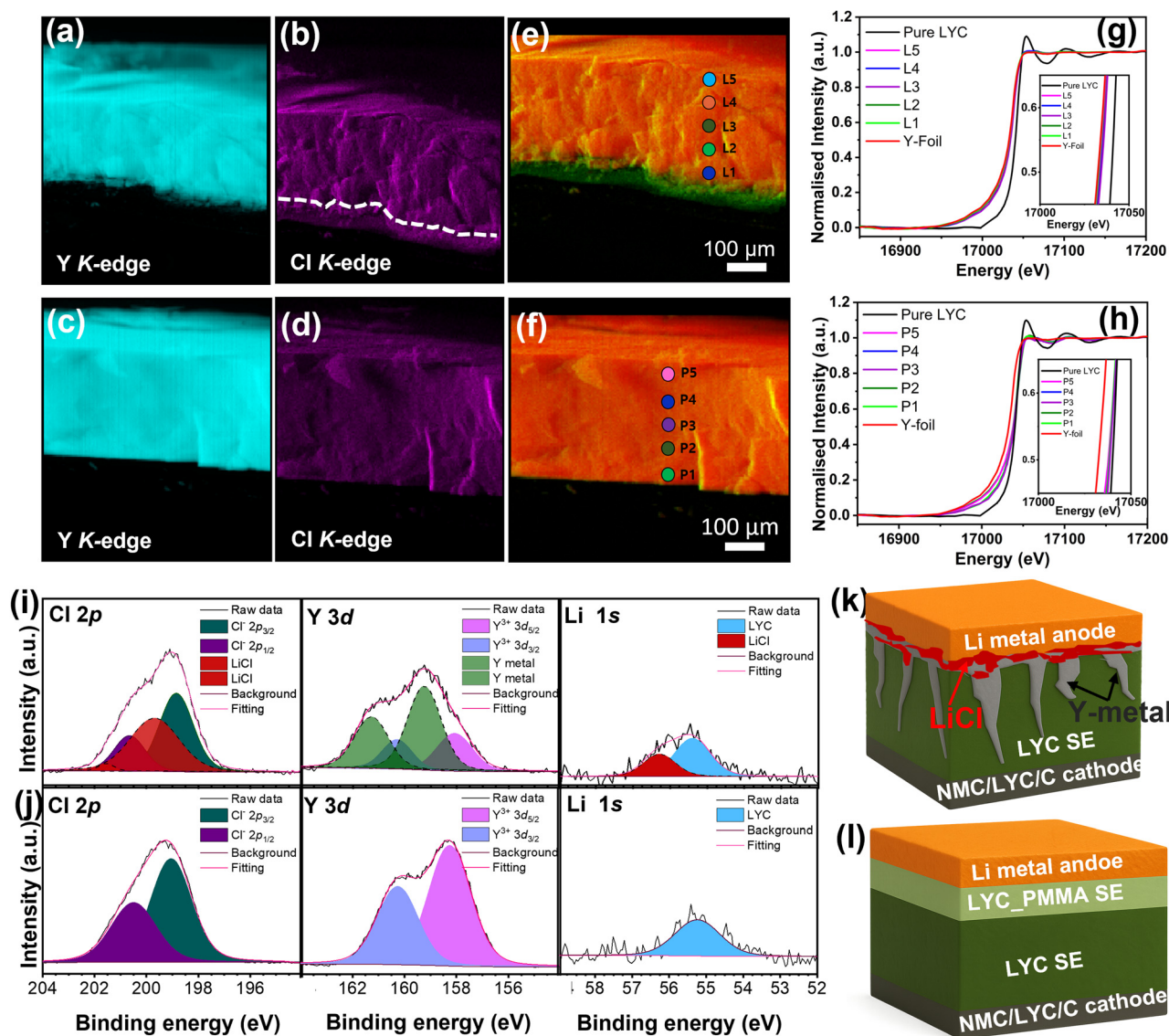
Fig. 5 μXRF maps of Y and Cl distribution on the electrolyte pellets recovered after continuous stripping/plating at a current density of 0.5 mA cm⁻²: (a and b) the Li|LYC|Li cell and (c and d) the Li|LYC_PMMA|Li cell. (e and f) Combined μXRF maps of Y and Cl collected from the Li|LYC|Li and Li|LYC_PMMA|Li cells, respectively. (g and h) Y-K edge hard XAS spectra collected at various locations of the cycled LYC and LYC_PMMA pellets, respectively. The locations are labelled in (e) and (f). (i and j) XPS profiles of Y 3d, Cl 2p, and Li 1s collected on the cycled LYC and LYC_PMMA, respectively. (k and l) Schematic figures showing the evolution of the anode interface upon cycling of the Li|LYC|NMC811 and Li|LYC_PMMA/LYC|NMC811 cells, respectively.

peaks attributed to metallic Y, whereas the same peaks do not appear in the cycled LYC_PMMA sample. This indicates that the reduction of Y³⁺ to metallic Y occurs only in LYC upon cycling. Similarly, the Cl 2p spectra of the pristine samples show two main peaks corresponding to Cl⁻ (2p₃/₂ and 2p₁/₂). After cycling, LYC exhibits additional peaks assigned to LiCl, while LYC_PMMA maintains only the original Cl⁻ peaks without any new features. In the Li 1s spectra, an additional peak corresponding to LiCl is detected in the cycled LYC, but not in the cycled LYC_PMMA. These results confirm the formation of LiCl at the interface of LYC and Li metal, whereas no LiCl is detected in the cycled LYC_PMMA. The presence of

the ionically conducting, electronically insulating PMMA interlayer prevents the direct contact between LYC and Li metal and the degradation reactions at the interface, consequently suppressing the formation of electronically conductive Y metal and LiCl side products. The stabilized interface enables prolonged stable cycling. In addition, the soft mechanical properties of PMMA promote better contact at the interface even at high current densities and low stack pressures.

Fig. 5k and l illustrate the distinctly different behaviors of LYC and LYC_PMMA SEs at the Li metal anode interface. In the LYC configuration, direct contact between Li-metal and LYC leads to significant interfacial degradation. This is mani-

fested as the severe propagation of the interfacial reactions that lead to LiCl formation and the reduction of Y^{3+} to Y^0, as well as the penetration of Y metal dendrites into the SE layer. These processes greatly compromise structural and electrochemical stability, leading to a rapid failure of the ASSB cell. The degradation mechanism is also consistent with the high impedance and increased resistance observed in the EIS spectra after cycling. In contrast, the use of the LYC_PMMA SE layer effectively suppresses these side reactions. The PMMA coating acts as a chemically inert and mechanically compliant interlayer that prevents direct contact between Li metal and the LYC surface. The interfacial protection is reflected in the EIS profile, where significantly lower impedance and minimal resistance growth are observed in the cycled LYC_PMMA ASSB cell. The stable interface results in improved Li^+ conduction and long-term electrochemical stability.

The effectiveness of the PMMA–LiTFSI coating in suppressing interfacial reactions can be attributed to several key factors. The coating layer is designed to be sufficiently thin, conformal, and electronically insulating to block parasitic charge transfer while still permitting Li^+ flux. This design is critical for preventing Li|LYC interfacial degradation, even under moderate stack pressures (<5 MPa). We believe three primary mechanisms contribute to its success. First, the polymer's negligible electronic conductivity and high dielectric strength make electron tunneling across the 4.3 nm film insignificant, thereby preventing reductive pathways such as $Y^{3+} \rightarrow Y^0$ and the formation of LiCl. Second, because the coating is only nanometers thick and contains a small fraction of LiTFSI, its area-specific ionic resistance (ASR) is low. With an estimated ionic conductivity (σ) of 10^{-7}–10^{-6} S cm^{-1} and a thickness (t) of 4.3 nm, the resulting ASR is approximately 0.4–4 Ω cm^2, a value well below typical interfacial resistances in halide systems. This ensures that Li^+ transport is not a rate-limiting step. Third, the amorphous and viscoelastic PMMA layer conforms intimately to the electrolyte surface under load. The applied stack pressure (∼5 MPa) is far below the yield stress of PMMA, which promotes uniform contact, homogenizes local stress, and mitigates the formation of voids that could otherwise nucleate filamentary failure.

This mechanistic understanding is consistent with our diagnostic results. Cyclic voltammetry shows strongly suppressed reduction currents compared to uncoated LYC. Furthermore, µXRF and XPS analyses detect no Cl-rich interphase or metallic Y in the coated sample after cycling. Finally, symmetric Li cells exhibit stable, low-polarization plating and stripping for over 1400 hours at 0.5 mA cm^{-2} under only ∼5 MPa of pressure. In summary, the nanometric polymer barrier functions as an electron-blocking, ion-permeable, and mechanically compliant interlayer, explaining how such a thin film can be highly effective under low stack pressures.

2.4. Air stability

It is well-known that sulfide SEs are sensitive to both oxygen and moisture upon air exposure,[40,41] which mandates their processing and handling inside a glovebox and adds signifi-

cant cost to manufacturing. While HSEs are generally stable against dry oxygen, recent studies have shown that irreversible damage occurs upon contact with moisture in the air, requiring them to be processed in the dry room.[42,43] For example, LYC was found to form a hydrate upon air exposure which further hydrolyzes during heat treatment.[44] The pristine material therefore cannot be easily recovered, necessitating engineering solutions to enhance its moisture stability. Here we show that PMMA coating also enhances the air stability of LYC and enables its handling and processing in air.

Fig. S8 and Fig. 6 compare the synchrotron *in situ* GIXRD patterns collected on the LYC and LYC_PMMA pellets, respectively, which monitor their structure changes during a given air exposure time (150 min). By changing the angles of the X-ray incident beam from 2° to 4° and to 6° (2θ), we gradually probe the pellet from the surface to the bulk, corresponding to a probing depth of approximately 6, 13, and 21 µm, respectively. It is evident that the GIXRD patterns of LYC measured at a 2° angle (Fig. S8a) showed immediate formation of the LiCl·H$_2$O and YCl$_3$·6H$_2$O phases, suggesting rapid surface degradation upon air exposure. Those collected at the 4° (Fig. S8b) and 6° (Fig. S8c) angles displayed a gradual increase in LiCl·H$_2$O and YCl$_3$·6H$_2$O peak intensities, confirming that the decomposition reaction initiates from the surface and progresses towards the bulk. In contrast, in the same series of GIXRD patterns collected on the LYC_PMMA pellet (Fig. 6a–c), no changes were observed, demonstrating exceptional air stability.

To further evaluate the effect of polymer coating on the air stability of halide solid electrolyte, *operando* time-resolved EIS was conducted on SS|LYC|SS and SS|LYC_PMMA|SS cells during an air exposure time of 40 hours (Fig. S9 and Fig. 6d). As shown in Fig. S9, the EIS profiles of the LYC cell display an initial increase in the impedance followed by a more pronounced gradual increase with increasing exposure time. In contrast, the corresponding profiles collected on the LYC_PMMA cell exhibited minimal changes in both bulk and interfacial resistance over time (Fig. 6d), indicating stable ionic transport throughout the exposure period. While LYC is known to undergo rapid degradation due to moisture-induced phase transformations, LYC_PMMA maintains its electrochemical stability due to the protective barrier of PMMA that suppresses moisture ingress and prevents the formation of hydrate species. These results confirm the effectiveness of the polymer coating in enhancing the environmental robustness of HSE, enabling their processing and handling under ambient conditions and eliminating the need for dry room conditions. Our approach, therefore, offers further advantages in processability and cost savings in ASSB manufacturing.

3. Experimental section

3.1. Material synthesis

To synthesize LYC, LiCl (Beantown Chemical, 99.9%) and YCl$_3$ (Thermo Scientific, 99.99%) were mixed in a stoichiometric ratio and ball-milled in a high-energy planetary ball mill
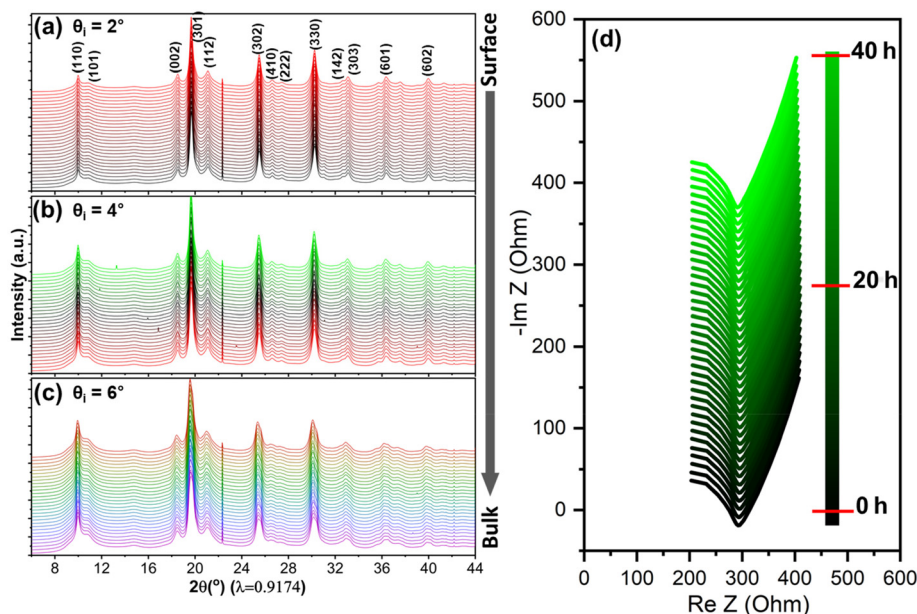
Fig. 6 Grazing-incidence XRD patterns of LYC_PMMA pellets as a function of air exposure time, collected at an incidence beam angle of (a) 2°, (b) 4°, and (c) 6° (2θ), respectively. The patterns were collected every 6 min within a total exposure time of 150 min. (d) *Operando* time-resolved EIS spectra of a symmetric SS|LYC_PMMA|SS cell recorded as a function of air exposure time to evaluate the air stability of LYC_PMMA SE.

(Retsch) at 600 rpm for 48 h. The precursor mixture (1.5 g) was added to a 50 ml ZrO_2 grinding jar with 12 ZrO_2 balls (10 mm) under an Ar atmosphere. During the milling process, the jar was opened under Ar to scrape the powder adhered to the wall before further milling. The resulting material was further homogenized by manual grinding in an agate mortar for 15 min. The polymer-modified halide solid electrolyte was synthesized under similar conditions. To enhance Li^+ conductivity, a small amount of LiTFSI (Sigma Aldrich) was incorporated into PMMA (M_w = 15 000 by GPC, Sigma Aldrich). The PMMA/LiTFSI composite (PMMA : LiTFSI = 85 : 15 wt%) was first prepared by ball milling at 300 rpm for 2 hours. Subsequently, a polymer coating was applied to LYC by mixing the PMMA composite with LYC and ball-milling at 300 rpm for 10 h. The weight ratio of PMMA + LiTFSI to LYC was controlled at 6 : 94.

3.2. Characterization studies

Powder X-ray diffraction was performed using a Bruker D2 Phaser equipped with a Cu Kα radiation (λ = 1.54184 Å). Synchrotron XRD in the transmission mode was performed at beamline 11-3 at SSRL with an X-ray wavelength of 0.974 Å. In both cases, samples were transferred into airtight holders inside a glovebox prior to the measurement to prevent air exposure. *In situ* GIXRD measurements were conducted at beamline 11-3 (SSRL) with 12.7 keV X-rays at various grazing angles to study air exposure effects. Scanning electron microscopy was conducted using a JEOL 7500F field emission SEM at 15 kV. Micro-X-ray fluorescence mapping and hard X-ray absorption spectroscopy were carried out at beamline 2-3 (SSRL). SE pellets were wrapped in Kapton foil prior to the measurement. X-ray photoelectron spectroscopy was per-

formed at 970 eV photon energy under high vacuum on cycled SE pellets. FTIR (Nicolet iS50 ATR) measurements were performed on powder samples in an ambient environment. TGA (NETZSCH, STA 449 F3) of powder samples was obtained under an Ar atmosphere at a scan rate of 10 °C min^{-1}.

Ionic conductivities of the samples were measured using ambient temperature electrochemical impedance spectroscopy in a stainless-steel split-cell equipped with either an LYC pellet (approximately 354 μm in thickness) or an LYC_PMMA pellet (approximately 400 μm in thickness). The pellets were prepared by pressing the powder samples at room temperature under an external pressure of 300 MPa for 5 min. All pellet pressing and handling during synthesis and cell assembly were carried out inside an Ar-filled glovebox (oxygen and water content <0.2 ppm). The AC impedance measurements were carried out in a frequency range of 7 MHz–100 mHz with a 10 mV perturbation. The ambient temperature was 20 ± 1 °C.

3.3. Electrochemical measurements

Cyclic voltammetry was conducted on cells with an HSE: Super C65 (70 : 30 wt%) composite as the working electrode and a Li-metal anode. The cells were cycled at room temperature in the voltage window of 0–2.5 V *vs.* Li/Li$^+$, at a scan rate of 0.1 mV s^{-1}. Li symmetric cells were assembled with a Li metal disc on both sides of the HSE and cycled at room temperature with an applied stack pressure of ~5 MPa.

Cathode composites were fabricated by hand grinding single-crystalline $LiNi_{0.8}Mn_{0.1}Co_{0.1}O_2$, SE powder, and a conductive carbon black in a weight ratio of 58 : 37 : 5. The ASSB cells were assembled inside a commercial solid-state cell using a bilayer SE configuration where the LYC layer (~300 μm) inter-

faces with the cathode and the LYC_PMMA layer (~100 μm) interfaces with the anode. The assembly was obtained using sequential pressing of the following: 70 mg of SE powder (300 MPa, 1 min), 10 mg cm^{-2} cathode composite (300 MPa, 5 min), and a 9 mm diameter Li foil disk (0.1 mm thick). Cells were cycled between 2.5 and 4.3 V *vs.* Li$^+$/Li under an external pressure of ~5 MPa. Stack pressure was determined from the applied force using a hydraulic press (YLJ-15, MTI Corporation) and a screw compression jig (EQ-YLJ-SP, MTI Corporation) with a pressure sensor. Galvanostatic cycling was performed using a VMP3 cycler (BioLogic), with 1C corresponding to 200 mAh g^{-1} for NMC811. All measurements were conducted at room temperature.

4. Conclusions

This study introduces polymer-modified halide solid electrolytes to address challenges related to the poor air stability, chemical stability, and interfacial compatibility of halide solid electrolytes with lithium metal anodes in ASSBs. A thin PMMA coating was applied to LYC particles utilizing a mechanochemical method, preserving the crystalline structure of LYC without inducing chemical modifications. The implementation of LYC_PMMA resulted in a substantial decrease in interfacial resistance and optimal operation at a low stack pressure of 5 MPa. Symmetric Li|SE|Li cells exhibited stable lithium plating/stripping over 1400 cycles at 0.5 mA cm^{-2}, with sustained low polarization. ASSB cells incorporating an uncoated NMC811 cathode and a lithium metal anode demonstrated high coulombic efficiency (~99.5%) and excellent capacity retention (~99%) after 100 cycles, contrasting with the rapid capacity degradation and significant polarization increases observed in cells using the pristine LYC. Synchrotron-based μ-XRF mapping and *ex situ* XPS analysis confirmed that the PMMA coating effectively inhibited the formation of decomposition products (LiCl and metallic Y) at the solid electrolyte interface. Furthermore, the PMMA layer markedly improved the air stability of LYC, enabling the prospect for ambient air processing of halide-based electrolytes and reducing fabrication costs associated with dry-room requirements. Our approach provides a scalable, cost-effective methodology to overcome major obstacles in halide SEs, thereby facilitating their integration into advanced high energy density ASSB systems.

Conflicts of interest

The authors declare no conflicts of interest.

Data availability

The data supporting this article have been included as part of the supplementary information (SI). SEM images, EDS line mapping, TGA, and XPS of LYC and LYC_PMMA. Conductivity measurement, temperature dependent Arrhenius plot of SS|LYC|SS and SS|LYC_PMMA|SS. EIS of different ball mill time and different coating of LYC_PMMA. Electrochemical performance of Cu|Li half-cells of LYC and LYC_PMMA. Stack pressure dependent EIS and EIS before and after cycling of bilayer ASSBs full cell with LYC and LYC_PMMA. GIXRD of LYC pellet as function of air exposure time, Operando time resolved EIS of SS|LYC|SS cell as function of air exposure time. See DOI: https://doi.org/10.1039/d5eb00134j.

References

1 M. Bianchini, A solid electrolyte with active stability: All-solid-state batteries, *Nat. Mater.*, 2025, 1–3, DOI: 10.1038/s41563-025-02323-6.

2 Z. Gao, H. Sun, L. Fu, F. Ye, Y. Zhang, W. Luo and Y. Huang, Promises, Challenges, and Recent Progress of Inorganic Solid-State Electrolytes for All-Solid-State Lithium Batteries, *Adv. Mater.*, 2018, **30**(17), 1705702, DOI: 10.1002/adma.201705702.

3 W. J. Kong, C. Z. Zhao, L. Shen, J. L. Li, Y. C. Le, X. Y. Huang, P. Xu, J. K. Hu, J. Q. Huang and Q. Zhang, From mold to Ah level pouch cell design: bipolar all-solid-state Li battery as an emerging configuration with very high energy density, *EES Batteries*, 2025, DOI: 10.1039/D5EB00126A.

4 X. Yu, R. Chen, L. Gan, H. Li and L. Chen, Battery Safety: From Lithium-Ion to Solid-State Batteries, *J. Eng.*, 2023, 9–14, DOI: 10.1016/j.eng.2022.06.022.

5 X. Yao, D. Liu, C. Wang, P. Long, G. Peng, Y. S. Hu, H. Li, L. Chen and X. Xu, High-Energy All-Solid-State Lithium Batteries with Ultralong Cycle Life, *Nano Lett.*, 2016, **16**(11), 7148–7154, DOI: 10.1021/acs.nanolett.6b03448.

6 L. Baggetto, R. A. H. Niessen, F. Roozehoom and P. H. L. Notten, High Energy Density All-Solid-State Batteries: A Challenging Concept towards 3D Integration,

Adv. Funct. Mater., 2008, **18**(7), 1057–1066, DOI: 10.1002/adfm.200701245.

7 D. L. Melvin, M. Siniscalchi, D. Spencer-Jolly, B. Hu, Z. Ning, S. Zhang, J. Bu, S. Marathe, A. Bonnin, J. Ihli and G. J. Rees, High plating currents without dendrites at the interface between a lithium anode and solid electrolyte, *Nat. Energy*, 2025, **1**, 1–10, DOI: 10.5281/zenodo.10523607.

8 J. Lee, T. Lee, K. Char, K. J. Kim and J. W. Choi, Issues and Advances in Scaling up Sulfide-Based All-Solid-State Batteries, *Acc. Chem. Res.*, 2021, **54**(17), 3390–3402, DOI: 10.1021/acs.accounts.1c00333.

9 S. Chen, D. Xie, G. Liu, J. P. Mwizerwa, Q. Zhang, Y. Zhao, X. Xu and X. Yao, Sulfide Solid Electrolytes for All-Solid-State Lithium Batteries: Structure, Conductivity, Stability and Application, *Energy Storage Mater.*, 2018, 58–74, DOI: 10.1016/j.ensm.2018.02.020.

10 Y. Zheng, Y. Yao, J. Ou, M. Li, D. Luo, H. Dou, Z. Li, K. Amine, A. Yu and Z. Chen, A Review of Composite Solid-State Electrolytes for Lithium Batteries: Fundamentals, Key Materials and Advanced Structures, *Chem. Soc. Rev.*, 2020, 8790–8839, DOI: 10.1039/d0cs00305k.

11 M. Shoji, E. J. Cheng, T. Kimura and K. Kanamura, Recent Progress for All Solid State Battery Using Sulfide and Oxide Solid Electrolytes, *J. Phys. D: Appl. Phys.*, 2019, **52**, 103001, DOI: 10.1088/1361-6463/aaf7e2.

12 X. Tang, F. Xie, X. Rong, Y. Lu, L. Chen and Y. S. Hu, Halide-based Solid Electrolytes:Opportunities and Challenges in Synergistic Development of All-Solid-State Li/Na Batteries, *EES Batteries*, 2025, DOI: 10.1039/D5EB00064E.

13 S. Yang, S. Y. Kim and G. Chen, Halide Superionic Conductors for All-Solid-State Batteries: Effects of Synthesis and Composition on Lithium-Ion Conductivity, *ACS Energy Lett*, 2024, **9**(5), 2212–2221, DOI: 10.1021/acsenergylett.4c00317.

14 Q. Wang, Y. Zhou, X. Wang, H. Guo, S. Gong, Z. Yao, F. Wu, J. Wang, S. Ganapathy, X. Bai, B. Li, C. Zhao, J. Janek and M. Wagemaker, Designing Lithium Halide Solid Electrolytes, *Nat. Commun.*, 2024, **15**(1), 1050, DOI: 10.1038/s41467-024-45258-3.

15 S. Y. Kim, S. M. Bak, K. J. Jun, G. Ceder and G. Chen, Revealing Dynamic Evolution of the Anode-Electrolyte Interphase in All-Solid-State Batteries with Excellent Cyclability, *Adv. Energy Mater.*, 2024, **14**(27), 2401299, DOI: 10.1002/aenm.202401299.

16 K. H. Park, S. Y. Kim, M. Jung, S. B. Lee, M. J. Kim, I. J. Yang, J. H. Hwang, W. Cho, G. Chen, K. S. Kim and J. Yu, Anion Engineering for Stabilizing Li Interstitial Sites in Halide Solid Electrolytes for All-Solid-State Li Batteries, *ACS Appl. Mater. Interfaces*, 2023, **15**(50), 58367–58376, DOI: 10.1021/acsami.3c13002.

17 L. M. Riegger, R. Schlem, J. Sann, W. G. Zeier and J. Janek, Lithium-Metal Anode Instability of the Superionic Halide Solid Electrolytes and the Implications for Solid-State Batteries, *Angew. Chem., Int. Ed.*, 2021, **60**(12), 6718–6723, DOI: 10.1002/anie.202015238.

18 A. Tron, A. Beutl, I. Mohammad and A. Paolell, Insights into the chemical and electrochemical behavior of halide and sulfide electrolytes in all-solid-state batteries, *Energy Adv.*, 2025, **4**, 518–529, DOI: 10.1039/D4YA00618F.

19 G. Zhang, X. Shi, Q. Su, Y. Sun, Y. Lu, K. Liu, Z. Li, H. Liu and L. Zhang, Halide-sulfide bilayer electrolytes for LiFePO4-based all-solid-state batteries, *Green Chem.*, 2024, **26**, 7971–7979, DOI: 10.1039/D4GC01640H.

20 T. Koç, M. Hallot, E. Quemin, B. Hennequart, R. Dugas, A. M. Abakumov, C. Lethien and J. M. Tarascon, Toward Optimization of the Chemical/Electrochemical Compatibility of Halide Solid Electrolytes in All-Solid-State Batteries, *ACS Energy Lett.*, 2022, **7**(9), 2979–2987, DOI: 10.1021/acsenergylett.2c01668.

21 A. Tron, A. Beutl, I. Mohammad and A. Paolella, Insights into the Chemical and Electrochemical Behavior of Halide and Sulfide Electrolytes in All-Solid-State Batteries, *Energy Adv.*, 2025, **4**, 518–529, DOI: 10.1039/D4YA00618F.

22 Z. Song, F. Chen, M. Martinez-Ibañez, W. Feng, M. Forsyth, Z. Zhou, M. Armand and H. Zhang, A reflection on polymer electrolytes for solid-state lithium metal batteries, *Nat. Commun.*, 2023, **14**, 4884, DOI: 10.1038/s41467-023-40609-y.

23 P. N. Didwal, Y. N. Singhbabu, R. Verma, B. J. Sung, G. H. Lee, J. S. Lee, D. R. Chang and C. J. Park, An advanced solid polymer electrolyte composed of poly (propylene carbonate) and mesoporous silica nanoparticles for use in all-solid-state lithium-ion batteries, *Energy Storage Mater.*, 2021, **37**, 476–490, DOI: 10.1016/j.ensm.2021.02.034.

24 S. Pazhaniswamy, S. A. Joshi, H. Hou, A. K. Parameswaran and S. Agarwal, Hybrid Polymer Electrolyte Encased Cathode Particles Interface-Based Core–Shell Structure for High-Performance Room Temperature All-Solid-State Batteries, *Adv. Energy Mater.*, 2023, **13**(1), 2202981, DOI: 10.1002/aenm.202202981.

25 P. N. Didwal, R. Verma, A. G. Nguyen, H. V. Ramasamy, G. H. Lee and C. J. Park, Improving Cyclability of All–Solid–State Batteries via Stabilized Electrolyte–Electrode Interface with Additive in Poly (propylene carbonate) Based Solid Electrolyte, *Adv. Sci.*, 2022, **9**(13), 2105448, DOI: 10.1002/advs.202105448.

26 Z. Li, R. Yu, S. Weng, Q. Zhang, X. Wang and X. Guo, Tailoring polymer electrolyte ionic conductivity for production of low-temperature operating quasi-all-solid-state lithium metal batteries, *Nat. Commun.*, 2023, **14**(1), 482, DOI: 10.1038/s41467-023-35857-x.

27 J. Zhang, J. Zhao, L. Yue, Q. Wang, J. Chai, Z. Liu, X. Zhou, H. Li, Y. Guo, G. Cui and L. Chen, Safety–reinforced poly (propylene carbonate)–based all–solid–state polymer electrolyte for ambient–temperature solid polymer lithium batteries, *Adv. Energy Mater.*, 2015, **5**(24), 1501082, DOI: 10.1002/aenm.201501082.

28 M. S. Su'Ait, A. Ahmad, H. Hamzah and M. Y. A. Rahman, Preparation and Characterization of PMMA-MG49-LiClO4 Solid Polymeric Electrolyte, *J. Phys. D: Appl. Phys.*, 2009, **42**(5), 055410, DOI: 10.1088/0022-3727/42/5/055410.

29 Y. L. Yap, A. H. You and L. L. Teo, Preparation and Characterization Studies of PMMA–PEO-Blend Solid Polymer Electrolytes with SiO2 Filler and Plasticizer for

Lithium Ion Battery, *Ionics*, 2019, **25**(7), 3087–3098, DOI: 10.1007/s11581-019-02842-8.

30 L. Yue, J. Ma, J. Zhang, J. Zhao, S. Dong, Z. Liu, G. Cui and L. Chen, All Solid-State Polymer Electrolytes for High-Performance Lithium Ion Batteries, *Energy Storage Mater.*, 2016, 139–164, DOI: 10.1016/j.ensm.2016.07.003.

31 F. Wu, K. Zhang, Y. Liu, H. Gao, Y. Bai, X. Wang and C. Wu, Polymer Electrolytes and Interfaces toward Solid-State Batteries: Recent Advances and Prospects, *Energy Storage Mater.*, 2020, **33**, 26–54, DOI: 10.1016/j.ensm.2020.08.002.

32 L. Jia, J. Zhu, X. Zhang, B. Guo, Y. Du and X. Zhuang, Li–Solid Electrolyte Interfaces/Interphases in All-Solid-State Li Batteries, *Electrochem. Energy Rev.*, 2024, **7**, 12, DOI: 10.1007/s41918-024-00212-1.

33 S. Ahmad, S. Ahmad and S. A. Agnihotry, Synthesis and Characterization of in Situ Prepared Poly (Methyl Methacrylate) Nanocomposites, *Bull. Mater. Sci.*, 2007, **30**(1), 31–35, DOI: 10.1007/s12034-007-0006-9.

34 S. Puls, E. Nazmutdinova, F. Kalyk, H. M. Woolley, J. F. Thomsen, Z. Cheng, A. Fauchier-Magnan, A. Gautam, M. Gockeln, S.-Y. Ham, M. T. Hasan, M.-G. Jeong, D. Hiraoka, J. S. Kim, T. Kutsch, B. Lelotte, P. Minnmann, V. Miß, K. Motohashi, D. L. Nelson, F. Ooms, F. Piccolo, C. Plank, M. Rosner, S. E. Sandoval, E. Schlautmann, R. Schuster, D. Spencer-Jolly, Y. Sun, B. S. Vishnugopi, R. Zhang, H. Zheng, P. Adelhelm, T. Brezesinski, P. G. Bruce, M. Danzer, M. El Kazzi, H. Gasteiger, K. B. Hatzell, A. Hayashi, F. Hippauf, J. Janek, Y. S. Jung, M. T. McDowell, Y. S. Meng, P. P. Mukherjee, S. Ohno, B. Roling, A. Sakuda, J. Schwenzel, X. Sun, C. Villevieille, M. Wagemaker, W. G. Zeier and N. M. Vargas-Barbosa, Benchmarking the Reproducibility of All-Solid-State Battery Cell Performance, *Nat. Energy*, 2024, **9**(10), 1310–1320, DOI: 10.1038/s41560-024-01634-3.

35 X. Hu, Z. Zhang, X. Zhang, Y. Wang, X. Yang, X. Wang, M. Fayena-Greenstein, H. A. Yehezkel, S. Langford, D. Zhou, B. Li, G. Wang and D. Aurbach, External-Pressure–Electrochemistry Coupling in Solid-State Lithium Metal Batteries, *Nat. Rev. Mater.*, 2024, 305–320, DOI: 10.1038/s41578-024-00669-y.

36 M. S. Diallo, T. Shi, Y. Zhang, X. Peng, I. Shozib, Y. Wang, L. J. Miara, M. C. Scott, Q. H. Tu and G. Ceder, Effect of Solid-Electrolyte Pellet Density on Failure of Solid-State Batteries, *Nat. Commun.*, 2024, **15**(1), 858, DOI: 10.1038/s41467-024-45030-7.

37 H. Guo, S. Zhong, L. Chen, G. Peng, F. Wang, T. Yan and J. Hu, Study on PVDF-HFP/PMMA/CMC Blended Polymer as Membrane for Lithium-Ion Batteries, *Int. J. Electrochem. Sci.*, 2022, **17**, 220145, DOI: 10.20964/2022.01.47.

38 S. Huo, L. Sheng, W. Xue, L. Wang, H. Xu, H. Zhang and X. He, Challenges of polymer electrolyte with wide electrochemical window for high energy solid-state lithium batteries, *InfoMat*, 2023, **5**, e12394, DOI: 10.1002/inf2.12394.

39 W. Ji, D. Zheng, X. Zhang, T. Ding and D. Qu, A kinetically stable anode interface for Li3YCl6-based all-solid-state lithium batteries, *J. Mater. Chem. A*, 2021, **9**, 15012–15018, DOI: 10.1039/D1TA03042F.

40 C. L. Singer, H.-C. Töpper, T. Kutsch, R. Schuster, R. Koerver and R. d. Daub, Hydrolysis of argyrodite sulfide-based separator sheets for industrial all-solid-state battery production, *ACS Appl. Mater. Interfaces*, 2022, **14**, 24245, DOI: 10.1021/acsami.2c01099.

41 Y.-T. Chen, M. A. Marple, D. H. Tan, S.-Y. Ham, B. Sayahpour, W.-K. Li, H. Yang, J. B. Lee, H. J. Hah and E. A. Wu, Investigating dry room compatibility of sulfide solid-state electrolytes for scalable manufacturing, *J. Mater. Chem. A*, 2022, **10**, 7155, DOI: 10.1039/D1TA09846B.

42 H. Kwak, S. Wang, J. Park, Y. Liu, K. T. Kim, Y. Choi, Y. Mo and Y. S. Jung, Emerging Halide superionic conductors for all-solid-state batteries: design, synthesis, and practical applications, *ACS Energy Lett.*, 2022, **7**, 1776, DOI: 10.1021/acsenergylett.2c00438.

43 X. Li, J. Liang, K. R. Adair, J. Li, W. Li, F. Zhao, Y. Hu, T.-K. Sham, L. Zhang and S. Zhao, Origin of Superionic Li3Y1−x In x Cl6 halide solid electrolytes with high humidity tolerance, *Nano Lett.*, 2020, **20**, 4384, DOI: 10.1021/acs.nanolett.0c01156.

44 Y. T. Chen, D. H. S. Tan, S. Y. Ham, B. Sayahpour, J. B. Lee, Y. Kim, M. Song, L. Nguyen, J. Oh, P. Ridley, A. Cronk, G. Deysher, J. Jang, Z. Chen and Y. S. Meng, Investigating Dry Room Compatibility of Chloride Solid-State Electrolytes for Scalable Manufacturing, *J. Electrochem. Soc.*, 2023, **170**, 080521, DOI: 10.1149/1945-7111/acee24.